JGR

Reducing nonuniqueness in finite source inversion using rotational ground motions

M. Bernauer[1], A. Fichtner[2], and H. Igel[1]

[1]Department of Earth and Environmental Sciences, LMU Munich, Munich, Germany, [2]Department of Earth Sciences, ETH Zurich, Zurich, Switzerland

Abstract We assess the potential of rotational ground motion recordings to reduce nonuniqueness in kinematic source inversions, with emphasis on the required measurement accuracy of currently developed rotation sensors. Our analysis is based on synthetic Bayesian finite source inversions that avoid linearizations and provide a comprehensive quantification of uncertainties and trade-offs. Using the fault and receiver geometry of the Tottori 2000 earthquake as a test bed, we perform inversions for two scenarios: In scenario I, we use translational velocity recordings only. In scenario II, we randomly replace half of the velocity recordings by rotation recordings, thus keeping the total amount of data constant. To quantify the noise-dependent impact of rotation recordings, we perform a sequence of inversions with varying noise levels of rotations relative to translations. Our results indicate that the incorporation of rotational ground motion recordings can significantly reduce nonuniqueness in finite source inversions, provided that measurement uncertainties are similar to or below the uncertainties of translational velocity recordings. When this condition is met, rupture velocity and rise time benefit most from rotation data. The trade-offs between both parameters are then strongly reduced, and the information gain nearly doubles. This suggests that rotational ground motion recordings may improve secondary inferences that rely on accurate information about rise time and rupture velocity. These include frictional properties of the fault, radiation directivity, and ground motion in general.

1. Introduction

1.1. Nonuniqueness in Finite Source Inversions

The kinematics of earthquake sources, i.e., the evolution of the rupture process in space and time on a finite fault, are key to our understanding of seismic hazard and earthquake dynamics. The inverse problem of inferring a kinematic source model from seismic data is ill posed, with solutions critically depending on (1) the parameterization of the model, (2) the inversion and regularization strategy, and (3) the available data [e.g., *Olson and Apsel*, 1982; *Hartzell and Heaton*, 1983; *Custodio et al.*, 2005; *Hartzell et al.*, 2007]. Furthermore, nonlinearities in the forward model, noisy data with insufficient coverage, and trade-offs between model parameters, result in a well-documented nonuniqueness of finite source models. Examples where different rupture scenarios explain observations equally well may be found, for instance, in *Olson and Anderson* [1988], *Beresnev* [2003], and *Ide et al.* [2005], as well as in the Blindtest on Earthquake Source Inversion, initialized within the E.U. Project SPICE (Seismic wave Propagation and Imaging in Complex media: a European network) [*Mai et al.*, 2007; http://equake-rc.info/].

To reduce nonuniqueness in finite source inversions, various authors proposed to complement traditionally used strong-motion recordings by other data, most importantly including various types of geodetic measurements [e.g., *Wald and Heaton*, 1994; *Hernandez et al.*, 1999; *Monelli et al.*, 2009].

Over the past decade, reliable measurements of rotational ground motions have become available, in addition to the traditionally used translational ground motion. This new data type motivates the present study, which aims to assess the potential of incorporating rotational ground motion measurements to better constrain kinematic rupture models.

1.2. Rotational Ground Motions

Rotational ground motion naturally complements classically observed translational ground motion in E-W, N-S, and vertical directions. Assuming infinitesimal deformation, the complete description of ground motion requires three components of translation, three components of rotation, and six components of strain

[e.g., *Aki and Richards*, 2002; *Cochard et al.*, 2006]. Rotation ω is defined through a linear combination of space derivatives of the translation vector $\mathbf{u} = (u_x, u_y, u_z)$:

$$\begin{pmatrix} \omega_x \\ \omega_y \\ \omega_z \end{pmatrix} = \frac{1}{2} \begin{pmatrix} \partial_x \\ \partial_y \\ \partial_z \end{pmatrix} \times \begin{pmatrix} u_x \\ u_y \\ u_z \end{pmatrix} = \frac{1}{2} \begin{pmatrix} \partial_y u_z - \partial_z u_y \\ \partial_z u_x - \partial_x u_z \\ \partial_x u_y - \partial_y u_x \end{pmatrix}. \tag{1}$$

Equation (1) suggests that the horizontal components of the rotation vector, known as tilt, effectively carry information on the seismic wavefield at depth that is not available from conventional arrays on the Earth's surface.

Rotational components of the seismic wavefield are naturally excited by earthquake source processes, including both slip and rotation on a fault [*Takeo and Ito*, 1997]. Furthermore, rotational motion results from the interaction of waves with 3-D heterogeneities and discontinuities.

In the past decade, numerous studies established rotational ground motion measurements as a new source of information. Their potential field of application is multifaceted and involves geophysical exploration, hazard assessment, and seismic engineering [e.g., *Takeo*, 1998; *Wang et al.*, 2009; *Stupazzini et al.*, 2009; *Zembaty*, 2009], as well as seismic tomography where the joint processing of translation and rotation data produces unique seismic observables with local sensitivities surrounding the receiver [*Fichtner and Igel*, 2009; *Bernauer et al.*, 2009, 2012b].

However, the rotational part of ground motion has been ignored for a long time primarily because of the lack of suitable measurement devices. Recently developed high-resolution ring-laser gyroscopes [*Schreiber et al.*, 2009b] produced the first consistent observation of teleseismic rotational ground motions in the vertical component, also known as torsion [*Igel et al.*, 2005, 2007]. With the development of fiber optic techniques, similar measurements for horizontal-component rotation are within reach [e.g., *Bernauer et al.*, 2012a; *Schreiber et al.*, 2009a; *Velikoseltsev et al.*, 2012].

1.3. Motivation and Outline

Here we anticipate the availability of six-component (6-C) seismic arrays, i.e., arrays that provide three components of translation (3-C) and three components of rotation data, and perform synthetic case studies to investigate the usefulness of such novel station networks for earthquake source inversion. The specific goals of this study are (1) to investigate if smaller 6-C arrays can provide more information on rupture processes than traditional 3-C arrays and (2) to quantify upper bounds of the admissible noise level in rotation recordings relative to translation recordings, needed to obtain additional constraints on finite source parameters. In this study we explicitly assume that rotation sensors are colocated with classical seismometers. This allows us to investigate the potential of rotational ground motions to reduce the number of station sites and hence the logistical effort in earthquake source studies.

To avoid bias by subjective regularization, we base our analyses on a Bayesian, i.e., probabilistic, inversion approach [*Sambridge and Mosegaard*, 2002; *Tarantola*, 2005]. This allows us to combine different data types in a natural way and to quantify the information gain that results from the incorporation of rotational ground motions with different noise levels. Former probabilistic studies on earthquake source parameters [e.g., *Peyrat and Olsen*, 2004; *Monelli et al.*, 2009; *Fichtner and Tkalcic*, 2010] already demonstrated that probabilistic methods are well applicable to inherently ill-posed finite source inverse problems.

This paper is organized as follows: In section 2, we introduce the parameterization of the model that we use in this study including the event geometry, the distribution of stations, and the representation of the fault plane. This leads to the formulation of the forward problem that defines the free parameters we invert for. As we primarily aim to study the impact of classic 3-C and novel 6-C data sets, we keep the rupture model and the forward solver deliberately simplistic. We describe the probabilistic source inversion approach in section 3, paying special attention to the assumed uncertainties in the data. Section 4 is dedicated to a series of synthetic case studies where we infer slip amplitudes, rupture velocity, and rise time. For this, we use the source-receiver geometry of the Tottori 2000 earthquake, for which various different rupture scenarios have been reported in the literature [e.g., *Iwata and Sekiguchi*, 2002; *Semmane et al.*, 2005; *Piatanesi et al.*, 2007; *Monelli et al.*, 2009]. We analyze one scenario exclusively based on 3-C data and compare the results to a second scenario including 6-C data at only half as many stations. We conclude with an assessment of the accuracy requirements of rotational ground motion sensors used in finite source inversion.
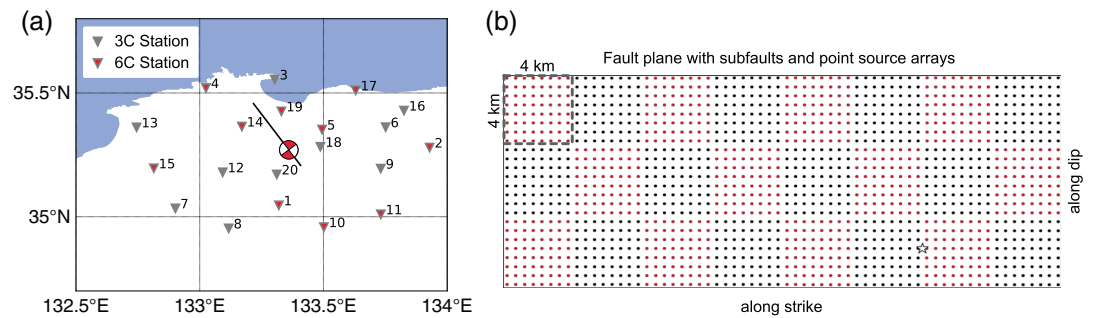
Figure 1. (a) Event geometry of the synthetic source inversion experiment based on the Tottori 2000 earthquake. Translational ground motions are simulated at all 20 stations (gray triangles). Triangles with a red marker symbolize a selection of 10 stations where both synthetic translation and rotation data are considered. The fault strike is described by the black solid line. The focal mechanism plotted at the epicenter location corresponds to a left-lateral strike slip event. (b) Vertically dipping fault plane divided into 24 quadratic subfaults with a side length of 4 km. Each subfault is represented by a regularly spaced pattern of 64 moment tensor point sources. The white star locates the hypocenter.

2. Kinematic Fault Rupture Modeling

In our synthetic source inversion experiments, we explore if 6-C seismic networks provide more information and thus reduce the nonuniqueness in finite source inversion compared to scenarios with only conventional 3-C arrays. To model a realistic test case, we implement the geometry of the M_w 6.7 Tottori, Japan, earthquake that occurred on 6 October 2000.

2.1. Scenario and Event Geometry

As the first major earthquake recorded by the K-/KiK-net strong-motion network (http://www.kik.bosai.go.jp/), the Tottori 2000 earthquake is well documented and intensively studied. The event exhibits a comparatively simple fault geometry, inferred mainly from aftershocks [*Fukuyama et al.*, 2003]. The focal mechanism is described by a left-lateral strike slip with a vertically dipping fault plane (dip = 90°, rake = 0°) striking at 150°, as illustrated in Figure 1a. Following the studies of *Semmane et al.* [2005] and *Monelli and Mai* [2008], we locate the hypocenter at 35.269°N, 133.357°E and 12.5 km depth; and we assume a buried fault plane with its upper edge at 2.75 km depth, 12 km dip length, and 32 km strike length. Fixing these parameters a priori, we do not invert for hypocenter coordinates, the moment tensor, and the geometry of the fault plane. The synthetic data used in the test are simulated at 20 sites corresponding to the locations of K-/KiK-net stations. The maximum receiver distance from the epicenter is 60 km (Figure 1a).

2.2. The Forward Problem

To kinematically describe the fault rupture evolution in time and space, we adopt the forward modeling approach used, for instance, by *Cotton and Campillo* [1995], *Hernandez et al.* [1999], or *Semmane et al.* [2005]. For this, we divide the fault plane into 24 quadratic subfaults with a side length of 4 km. Each subfault consists of 64 regularly spaced moment tensor point sources, thus resulting in a grid spacing of 0.5 km (Figure 1b). We compute the 6-C response (velocities and rotation rates) up to a frequency of 1 Hz for each point source. For the wavefield simulations we use the 1-D purely elastic Earth model proposed by *Semmane et al.* [2005] and also used by the Research Center for Earthquake Prediction of the Disaster Prevention Research Institute, Kyoto (see Appendix A). To be flexible for potentially more complex models in future studies, we applied a spectral element solver to compute the seismic wavefield for the moment tensor point sources on each subfault [*Fichtner et al.*, 2009]. With a minimum wavelength of 3179 m, this setup is similar to the previous kinematic source studies by *Cotton and Campillo* [1994, 1995] who propose a subfault length at the order of the shortest wavelength, with at least six-point sources in vertical and horizontal direction. In our model the rupture propagates only horizontally with a fixed mesoscopic rupture velocity of 2500 m/s on each subfault. We compute a library with the seismic response of each subfault by summing over the previously computed point source seismograms in each subfault, appropriately delayed in time. This library has to be computed only once and contains the seismic wavefield, G^r_{kl}, corresponding to subfault k, station r, and component l.

The rupture of the subfault is triggered when the macroscopic rupture front reaches the subfault center. We allow each subfault to slip once and parameterize the slip process in terms of slip amplitude ($slip_k$),
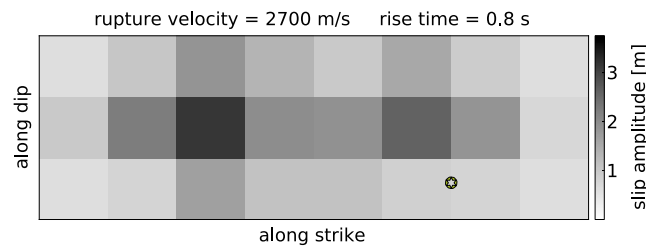
Figure 2. Heterogeneous slip amplitude distribution of the target model. Two-slip amplitude peaks of 3.2 m and 2.6 m are centered in the left and the right half of the rupture plane. Rupture velocity (2700 m/s) and rise time (0.8 s) are homogeneous across the fault plane. The hypocenter is marked by a white star.

macroscopic rupture velocity (c^{rup}), and rise time (R). The slip amplitude is heterogeneous across the fault plane, leading to 24 free parameters. Together with the distance between the center of subfault k and the hypocenter, the rupture velocity provides the rupture time $t_k(c^{rup})$ of subfault k. The rise time expresses the duration of the slip. Both rupture velocity and rise time are homogeneous parameters across the fault plane. Thus, we invert for 26 free parameters in total. Finally, the complete seismic response, $v_l^r(\omega)$, at station r, component l, and for the circular frequency, $\omega = 2\pi f$, is computed as a linear sum of $N(= 24)$ subfault contributions

$$v_l^r(\omega) = \sum_{k=1}^{N} \text{slip}_k \exp\left[-i\omega\, t_k(c^{rup})\right]\, G_{kl}^r(\omega)\, S(R, \omega). \qquad (2)$$

In equation (2) S represents the source function that we implemented as an ordinary ramp function. Additional details on the source function are provided in Appendix B.

2.3. Target Model and Synthetic Data

Performing a synthetic study means that we know the true kinematic rupture model (target model) we invert for in advance. Mimicking the results of former studies on the Tottori 2000 event [e.g., *Semmane et al.*, 2005; *Monelli and Mai*, 2008], we assume a heterogeneous distribution of slip amplitudes with two high-slip regions (asperities), as visualized in Figure 2. As realistic values for rupture velocity and rise time we use 2700 m/s and 0.8 s, respectively. Inserting the target model into equation (2) yields the synthetic data that we try to fit in the inversion process. Figure 3 shows some characteristic features of the synthetic data produced by the target model. For each station, the energy ratios, i.e., the L_2 norm ratios of the seismograms, observed in fault parallel (gray), fault normal (black), and vertical (orange) components are displayed. Figure 3a corresponds to velocity and Figure 3b to rotation rate seismograms, respectively. Different values of the absolute energy measured at individual stations are encoded in the circle diameter at each station and are explained mainly by the station distance to the fault and the focal mechanism. As expected for a strike-slip event, Figure 3 highlights that velocity measurements provide the highest energy in the horizontal components. For example, at station 6, 7, 10, 15, or 16 the energy measured in the vertical components almost tends to zero. For rotation rates, the highest energy is mostly found in the vertical components, but
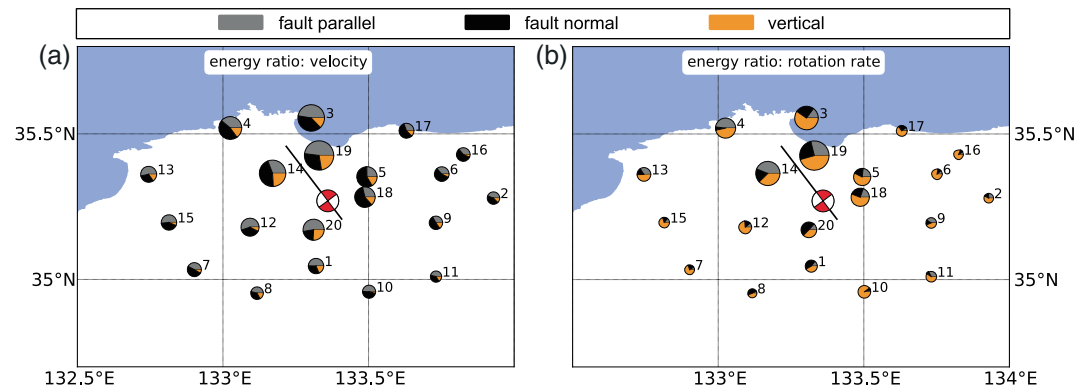

Figure 3. Energy ratios corresponding to fault parallel (gray), fault normal (black), and vertical (orange) component seismograms. The circle diameter reflects the absolute energy values in the synthetic data for each station. (a) Concerning velocity seismograms, the highest energy is observed in the horizontal components. (b) Rotation rates provide the highest energy mostly in the vertical components even though at several stations considerable energy is present also in the horizontal components.
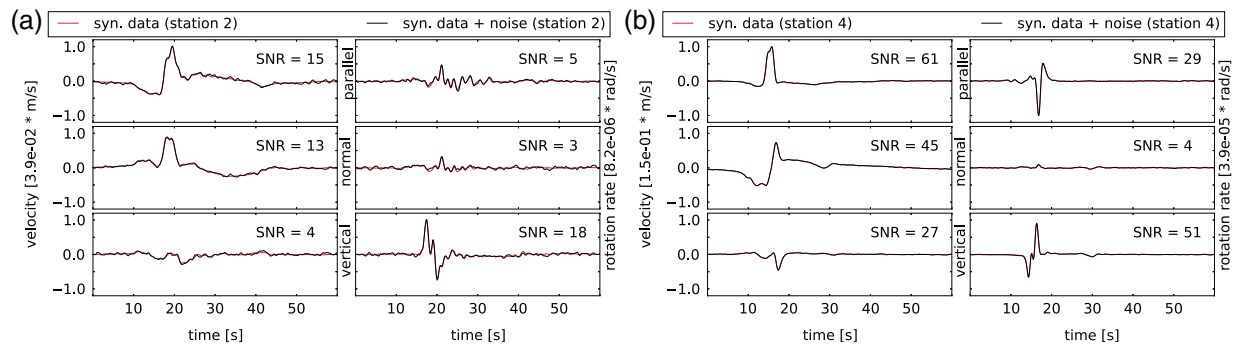
Figure 4. Synthetic data (red) and synthetic data perturbed with Gaussian noise (black). (a) Fault parallel, normal, and vertical seismograms and their corresponding signal-to-noise ratio (SNR) are plotted for (left) velocity and (right) rotation rate observations at station 2. (b) The same as Figure 4a but for station 4.

there are also stations with considerable energy in tilt as, for example, stations 1, 9, 14, 19, and 20. This concentration of energy in the horizontal velocity and vertical rotation rate seismograms is distinctive for a strike-slip event.

To render our synthetic study more realistic, we add Gaussian noise to each synthetic seismogram. Note that our wave equation solver directly computes translation and rotation seismograms for the moment tensor point sources. This enables us to perturb each seismogram independently. Hence, the noise on the translational and rotational components is not correlated. Since we limit our analysis to a comparison of finite source inversions with and without rotational ground motions, only the relative noise level in translational and rotational seismograms is relevant. In our initial examples, we set equal noise levels in translations and rotations, with an amplitude of 1.0% of the maximum amplitude observed in all velocity and rotation rate synthetics, respectively. This choice ensures that a potential gain (or loss) of information from any type of data does not result from different noise levels. In section 4.4 we perform studies with varying noise levels in the rotation recordings, thus exploring the requirements on measurement accuracy.

Figure 4 demonstrates how the additional Gaussian noise affects the synthetic data. Station 2 (Figure 4a) is one of the large-distance stations and represents low-amplitude data. The signal-to-noise ratio (SNR), i.e., the ratio between maximum data and noise amplitudes, varies between 3 and 18, depending on the component. For stations closer to the fault, the noise is negligible, as illustrated for station 4 in Figure 4b.

3. Probabilistic Finite Source Inversion

Finite source inversion is ill posed due to the sparsity of data, the presence of noise, and the nonlinear relationship between model parameters and data.

Deterministic source inversion attempts to find the model that best explains the data, typically using iterative optimization techniques. The lack of information with its resulting nonuniqueness is compensated by regularization, e.g., in the form of smoothing and damping. Since regularization is to some degree subjective, resolution estimates tend to be biased [*Trampert and Fichtner*, 2013]. Furthermore, the existence of multiple plausible solutions that explain the data equally well is not taken into account.

Though computationally more expensive, probabilistic (or Bayesian) source inversion overcomes the drawbacks of the deterministic approach using a global model search that provides unbiased measures of resolution and trade-offs. Since reliable resolution analyses are essential for our study, we thus decided to apply a Bayesian approach.

3.1. Bayesian Inverse Theory
In the following we summarize Bayesian finite source inversion, using the concepts described, for instance, in *Mosegaard and Tarantola* [1995] and *Tarantola* [2005]: We combine the available prior knowledge on the model parameters, the observations, and the theoretical relationship between model parameters and data into the solution of the inverse problem in the form

$$\sigma(\mathbf{m}) = k\,\rho(\mathbf{m})\,L(\mathbf{m}). \tag{3}$$

In equation (3), k is a normalization constant, $\mathbf{m}$ denotes an element of the (26-dimensional) model space, $\rho(\mathbf{m})$ represents the prior information on the model parameters in terms of a multidimensional probability density function (*prior pdf*), and the likelihood function $L(\mathbf{m})$ provides a measure of how well a model $\mathbf{m}$ explains the data $\mathbf{d}$. Consequently, the solution or posterior state of information, $\sigma(\mathbf{m})$, is given in terms of a multidimensional probability density function (*posterior pdf*).

3.2. Prior Information and Likelihood Function

As priors in model space we use probability densities that are constant within a prescribed interval. Furthermore, different model parameters m^α ($\alpha = 1, 2, ..., 26$) are initially assumed to be independent. The index α refers either to slip amplitude, rise time, or rupture velocity. It follows that the full prior in the model space is given by

$$\rho(\mathbf{m}) = \prod_\alpha \rho_\alpha(m^\alpha),\tag{4}$$

with

$$\rho_\alpha(m^\alpha) = \begin{cases} (m^\alpha_{\max} - m^\alpha_{\min})^{-1}, & \text{for} \quad m^\alpha_{\min} \leq m^\alpha \leq m^\alpha_{\max} \\ 0, & \text{otherwise.} \end{cases}$$

For the intervals $[m^\alpha_{\min}, m^\alpha_{\max}]$ we use $[0, 5]$ m for the slip amplitude, $[0.5, 1.5]$ s for the rise time, and $[2000, 3000]$ m/s for the rupture velocity. Assuming negligible forward modeling errors, we employ the exponential likelihood function

$$L(\mathbf{m}) = k' \exp\left[-\sum_l \left(\frac{\chi_l(\mathbf{m})}{s_l}\right)\right],\tag{5}$$

where k' is again a normalization constant. In equation (5), $\chi_l(\mathbf{m})$ denotes the measure of misfit between data predicted from the model and the observed data, and s_l represents the noise level. The index l refers to either velocity or rotation rate recordings. We calculate the misfit based on the L_2 norm as

$$\chi_l(\mathbf{m}) = \frac{1}{2} \sum_r \left(\mathbf{g}^r_l(\mathbf{m}) - \mathbf{d}^r_{l,\text{obs}}\right)^2.\tag{6}$$

The symbols $\mathbf{g}^r_l(\mathbf{m})$ and $\mathbf{d}^r_{l,\text{obs}}$ denote the forward modeling function and the (synthetic) data at station r, respectively. We underline that the noise level is a natural weight, balancing in equation (5) the summation of misfits computed for diverse observations. Hence, the probabilistic inversion approach automatically accounts for different data types like velocity and rotation rate seismograms.

3.3. The Metropolis Algorithm

To approximate the *posterior pdf*, probabilistic inversions use random walks through the model space. The specific implementation of this sampling process depends on the individual problem under investigation. As our forward problem can be solved efficiently for a large number of models, and because the dimension of the model space is small, we can apply a Metropolis-Hastings algorithm [*Metropolis and Ulam*, 1949; *Metropolis et al.*, 1953; *Hastings*, 1970]. For this, we produce a candidate model, $\mathbf{m}_{\text{can}}$, that samples the *prior pdf*. The candidate model is then included in the final ensemble of models with an acceptance probability P_{accept} that depends on the current model $\mathbf{m}_{\text{cur}}$

$$P_{\text{accept}} = \begin{cases} 1, & \text{if } \chi(\mathbf{m}_{\text{can}}) \leq \chi(\mathbf{m}_{\text{cur}}) \\ \frac{L(\mathbf{m}_{\text{can}})}{L(\mathbf{m}_{\text{cur}})}, & \text{if } \chi(\mathbf{m}_{\text{can}}) > \chi(\mathbf{m}_{\text{cur}}), \end{cases}\tag{7}$$

with

$$\chi(\cdot) = \sum_l \left(\frac{\chi_l(\cdot)}{s_l}\right).\tag{8}$$

Hence, the candidate model is always accepted if it improves the data fit, but if the candidate model degrades the data fit there is still a chance of not being rejected. The ensemble of accepted models can be displayed in the form of histograms, where the height of a column is proportional to the posterior likelihood.
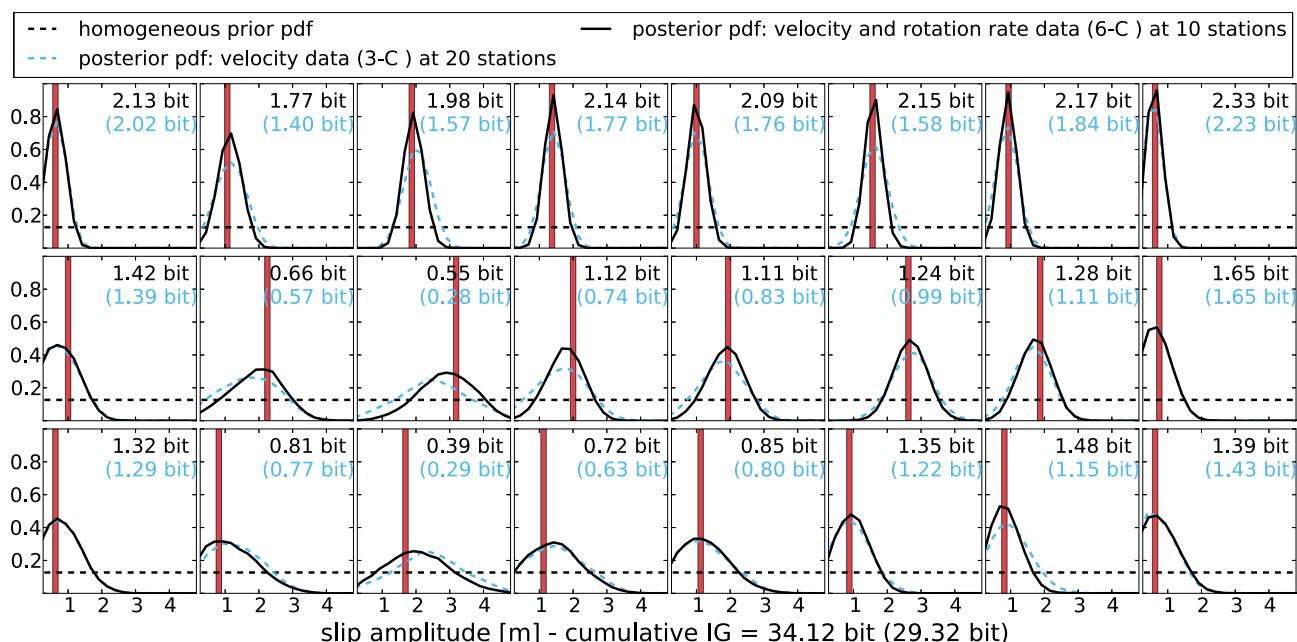
Figure 5. Inversion results for the slip amplitude. Each panel represents one subfault of the rupture plane arranged equivalent to Figure 2, while every subplot shows the *prior pdf* (black dashed line) and the true value of the target model (red bar). The blue dashed lines correspond to the *posterior pdf*s in scenario I (3-C velocity data at 20 stations). Black lines show the same but for scenario II (6-C velocity and rotation rate data at 10 stations). The black and blue numbers describe the information gain (blue: scenario I, black: scenario II).

3.4. Shannon's Measure of Information Gain

Once the sampling algorithm has converged to the *posterior pdf*, we can quantify the information content or information gain relative to the prior. Following *Tarantola* [2005], we define the information gain for a specific inversion scenario as the relative information content of the *posterior pdf*, ρ, with respect to the *prior pdf*, σ, as

$$I(\rho; \sigma) = \int \rho(x) \log \left[\frac{\rho(x)}{\sigma(x)} \right] \, dx. \tag{9}$$

We use the logarithm base 2 in equation (9), so the unit of information gain is termed a *bit*.

4. Case Studies With and Without Rotations

In this section we aim to recover rupture velocity, rise time, and the 24 slip amplitude parameters of the target model, described in section 2.3, using the previously introduced probabilistic inversion technique. We study two different scenarios: In scenario I, we use the conventional 3-C velocity data of all 20 stations shown in Figure 1a. In scenario II, we also include rotational ground motions but only consider 10 stations.

At this point, we emphasize two important aspects: (1) The information gain that we analyze in both scenarios is based on the same number of seismograms (66). This means that the pure quantity of data is the same. (2) The 10 stations in scenario II are randomly selected. First, for the purpose of easy illustration, we consider only one possible selection of 10 out of 20 stations (section 4.2). To assess the extent to which results depend on a particular selection, we then repeat the inversion for a large number of station subsets (section 4.3).

4.1. Scenario I: Inverting 3-C Velocity Observations at 20 Stations

In scenario I, we invert 3-C velocity seismograms at all 20 stations. Applying the Metropolis rule from section 3.3 to 1 million test models, we approximate the *posterior pdf*. The 24 marginal *posterior pdf*s for the slip amplitudes are plotted in Figure 5, where each panel represents a subfault of the rupture plane, arranged as in Figure 2. Each subplot shows the *prior pdf* as black dashed line, and the slip value of the target model as red bar. The blue dashed lines correspond to the *posterior pdf*s. Blue numbers in brackets describe the information gain for each parameter according to equation (9).
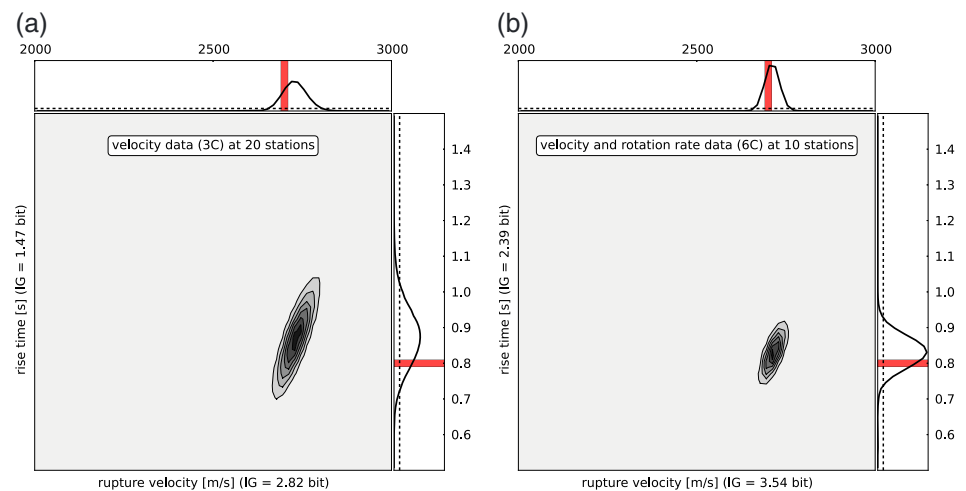
Figure 6. Inversion results for rupture velocity and rise time. The 2-D marginal *posterior pdf*s express the cross dependency between rupture velocity and rise time. The corresponding 1-D marginal *posterior pdf*s are drawn at the top and to the right of each panel for rupture velocity and for rise time, respectively. (a) The dark gray and black-shaded areas mark the relatively large region where both parameters compensate each other during the inversion process of scenario I. (b) The area of cross dependencies between rise time and rupture time decreases substantially in scenario II.

With an average of 1.77 bit, the information gain in the top row of subfaults is largest, indicating that near-surface slip amplitudes are resolved best. Their *posterior pdf*s have well-defined peaks matching the true parameters. In the middle part of the fault plane (middle row), the information gain for slip amplitudes reaches slightly more than 50% (0.95 bit on average) compared to the values observed in the top row. The same is approximately true for the bottom of the fault plane (bottom row).

A reliable estimate of the target slip is not feasible from several *posterior pdf*s in the middle and the bottom rows of the fault plane. This indicates that strong motion waveforms are mostly sensitive to rupture near the surface and relatively insensitive to rupture at greater depth, in accord with previous studies [e.g., *Mendoza and Hartzell*, 1989; *Cotton and Campillo*, 1995; *Semmane et al.*, 2005; *Monelli and Mai*, 2008]. Considering top, middle, and bottom rows of the rupture plain individually, we observe a general decrease of information gain at greater distances from the hypocenter. Moreover, we attribute variations in the information content along the strike direction of the rupture plane to the irregular distribution of stations at the surface (directivity effect).

The inversion results for rupture velocity and rise time are visualized in Figure 6a in the form of a 2-D marginal that reveals the trade-offs between these two parameters. The dark gray and black-shaded areas mark the relatively large region where variations in both parameters compensate each other, so as to have nearly no effect on the misfit. The corresponding 1-D marginal *posterior pdf*s are drawn at the top for rupture velocity and to the right for rise time, respectively. Evidently, the expected values of both approximately bell-shaped *posterior pdf*s miss the target model, which is especially true for the rise time.

Analyzing the seismogram fit in scenario I further motivates the inclusion of rotational ground motion observations in the following scenario II. In Figure 7 we compare the seismograms at station 10 for the target model (black line) and for a model randomly chosen from the 1% of models with the lowest misfit (red line). The top and the bottom rows of Figure 7 show velocity and rotation rate seismograms, respectively. Each component is characterized by the normalized L_2 misfit between synthetics and observations. As in the inversion process of scenario I only velocity seismograms are fitted, we observe a substantially higher L_2 misfit in rotation rate seismograms compared to velocity seismograms. The L_2 misfit of the vertical rotation rate seismograms is, for example, twice as large as the misfit in both horizontal velocity seismograms. This indicates the potential of inverting the source parameters including rotation rate seismograms. Figure 7 suggests that additional contributions from rotational ground motions may come mainly from their amplitudes, as the phases of observed and synthetic seismograms are already in good agreement.
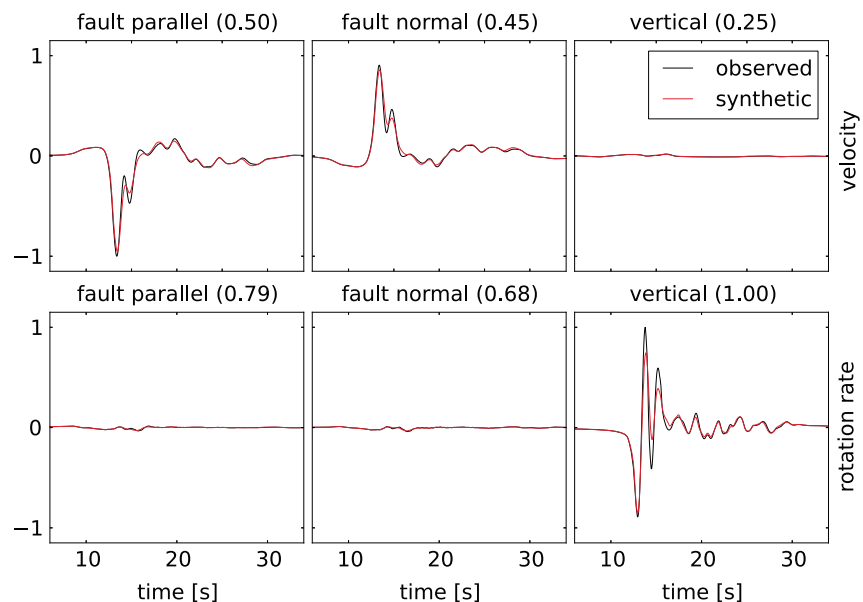
Figure 7. Normalized seismograms at station 10 produced by a model selected from the 1% best data fitting model samples. The numbers in brackets represent the normalized L_2 misfits between observed (black line) and synthetic (red line) seismograms. The maximal amplitude for nonnormalized velocity and rotation rate seismograms is 10.1 cm/s and 3.1×10^{-5} rad/s, respectively.

4.2. Scenario II: Inverting 6-C Observations at 10 Stations

In contrast to scenario I, scenario II combines velocity and rotation rate observations. To keep the total amount of data in the inversion constant, we randomly select 10 stations from the complete array. These are marked as red triangles in Figure 1a. Despite considering 6-C data at 10 stations instead of 3-C data at 20 stations, the inversion is performed with the identical parameter setup compared to scenario I.

We obtain the following results: The *posterior pdf*s of the slip amplitude (Figure 5, solid black lines) in the top row subfaults acquire sharper peaks, accurately matching the target model values. Analogously to scenario I, the information gain decreases with depth. Nevertheless, 6-C observations compared to 3-C observations provide a higher information gain for slip amplitude for almost all subfaults, despite using only half as many stations. In numbers, the cumulative information gain for slip amplitude is 34.12 bit in scenario II. In scenario I, this value equals 29.32 bit, i.e., 86% of what is obtained in scenario II.

Using 6-C data at 10 stations significantly sharpens the *posterior pdf*s for rise time and rupture velocity, as shown in the 2-D marginal of Figure 6. Trade-offs between the parameters are strongly reduced, and the peaks of the 1-D marginal *posterior pdf*s are close to the target values. Compared to scenario I, the information gain in scenario II is 25% larger for rupture velocity and more than 60% larger for rise time. However, discrepancies between the correct input values and the expected values of the *posterior pdf*s remain also in scenario II.

For a visual inspection of low misfit models accepted during the inversion process of scenario II, we refer to Appendix C, Figure C1. The ensemble of models highlights the relation between the observed information gain and the degree of variability in the model parameters. However, it also proves that a sophisticated evaluation of probabilistic inversion results is not feasible by the inspection of individual models. In Appendix C (Figure C2), the seismograms corresponding to the models from the ensemble are compared to the seismograms produced by the target model for all stations used in scenario II.

4.3. Generalization: Random Selection of Stations

The inversion of source parameters in scenario II suggests that including rotational ground motion measurements reduces the nonuniqueness of finite source inversions. To ensure that information gain does not result from merely increasing the quantity of data, we only used 10 stations for the 6-C inversion, thus keeping the same total number of seismograms as in the 3-C scenario with 20 stations.
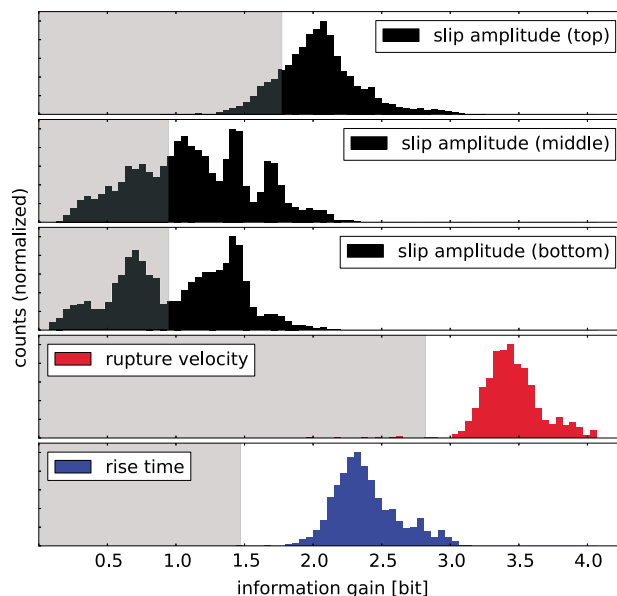
Figure 8. Histograms for the information gain corresponding to 1000 scenarios inverting 6-C observations at 10 randomly selected stations. (first to third panels) Black histograms correspond to the average information gain of slip amplitudes for subfaults of the fault plane. Histograms for rupture velocity and rise time are plotted in (fourth panel) red and (fifth panel) blue, respectively. For comparison the information gain of scenario I is indicated by the end of the gray bar. Thus, only the scenarios on white background benefit from using rotational ground motions.

Repeating the inversion procedure for 1000 randomly selected combinations of 10 stations allows us to assess the generality of our results. Figure 8 displays the average information gain for slip amplitudes in the first, second, and third panels of the fault plane, and the information gain for rupture velocity and rise time for all of the 1000 probabilistic inversions based on 6-C data. The information gain for the 3-C inversion with 20 stations is shown for comparison. Using 6-C data at 10 stations almost always provides more information than using 3-C data at 20 stations, regardless of which combination of 10 stations is used. This effect is most pronounced for slip amplitude in the first row of subfaults, rupture velocity, and rise time.

Only for some station combinations the information gain is lower, probably because the randomly selected stations may lead to large azimuthal gaps in the station distribution. Also, the random selection may contain little energy in horizontal rotation rate components, that we consider essential for reducing the nonuniqueness.

As seen in the second and the third panels of Figure 8 this strongly affects the less resolved slip amplitudes in the second and third panels of the fault plane. The histograms provide several peaks in contrast to the well-resolved parameters indicating that the station distribution is critical for slip at greater depth.

At this point, we conclude that the nonuniqueness in finite source inversions can be significantly reduced by including rotational ground motion measurements. We emphasize that only the combination of both data types, velocity and rotation rate seismograms, leads to the benefits described above. Inverting rotation rate seismograms separately for all stations resembled the results corresponding to scenario I.
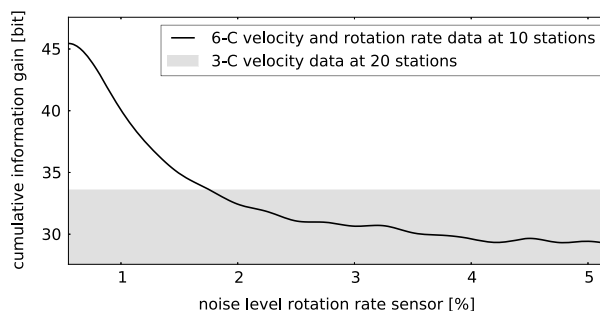
4.4. Requirements on the Measurement Accuracy of Rotational Ground Motion Sensors

It remains to be investigated which level of measurement accuracy rotational ground motion sensors must provide so that finite source inversion can benefit from the novel data type.

To address this question, we consider again the setup of scenario II, and we perform the same inversion process as described in section 4.2 with varying noise levels in the rotation rate data. Since the information gain of 6-C relative to 3-C inversions is controlled by the ratio between

Figure 9. Cumulative information gain corresponding to different noise levels in the rotation rate sensors and constant noise level in the velocity observations. For comparison the cumulative information gain received in scenario I that inverts only velocity seismograms is indicated by the gray bar.

velocity and rotation rate noise levels, we keep the noise level in velocity seismograms constant at 1% of the maximum amplitude of all velocity seismograms.

In a first scenario, we contaminate the rotation rate synthetics with Gaussian noise that has an amplitude 0.5% of the maximum rotation rate amplitude at all stations, i.e., half the noise amplitude of scenario II. As illustrated in Figure 9, this results in a cumulative information gain for all parameters of 45 bit, compared to 33 bit in scenario I. The cumulative information gain of scenario II (1% noise) equals 40.48 bit. Considering various scenarios with increasing noise levels in the rotation rates provides the black curve in Figure 9. As expected, increasing the noise level in the rotation rates decreases the cumulative information gain. When the rotation rate noise level reaches 1.75%, the cumulative information gain drops to the one of scenario I, meaning that the potentially available additional information is full compensated by measurement errors. For a noise level of 5% the cumulative information gain is already lower than 30 bit.

In summary, our test with varying noise levels suggests that the signal-to-noise ratio in rotation rate recordings should be similar to the one in velocity recordings in order to be beneficial for finite source inversions.

5. Discussion

The main result of this study is that the incorporation of rotational ground motion data into kinematic source inversion can significantly reduce nonuniqueness, provided that measurement errors in rotation data are roughly at the same level as errors in classical translation data. This result must be seen in the light of the following aspects that we discuss below: (1) The availability of current and the construction of future rotation sensors, (2) the physical origin of the observed information gain, (3) the potential implications for earthquake physics and ground motion predictions, and (4) the inversion technique used in this study.

5.1. Measuring Rotational Ground Motions
While the vertical component of rotational ground motion can be approximated via finite differences from translational recordings at the surface, a similar approximation of the horizontal components would require borehole seismometers that are mostly unavailable. Alternatively, the seismogeodetic method [*Bodin et al.*, 1997; *Spudich et al.*, 1995; *Spudich and Fletcher*, 2008] may be used to derive rotational ground motion from translation recordings at the surface [e.g., *Suryanto et al.*, 2006; *Kendall et al.*, 2012; *Pham et al.*, 2012]. This method requires, however, detailed knowledge of 3-D subsurface structure. In any case, the derivation of rotations from translations relies on the availability of a sufficiently dense array where the interstation spacing is shorter than the minimum wavelength. This condition would not be met in our study where the shortest wavelength is around 3 km.

A high-resolution, field deployable, and affordable instrument that measures rotation is currently not available. However, the construction of rotation sensors based on ring-laser technology [e.g., *Schreiber et al.*, 2009a, 2009b; *Velikoseltsev et al.*, 2012], adapted gyroscopes [e.g., *Bernauer et al.*, 2012a], or systems of multiple geophones [e.g., *Brokešová and Málek*, 2010; *Brokešová et al.*, 2012] is rapidly progressing. In the course of these instrument developments, the admissible measurement errors for specific applications must be established. To be beneficial in finite source studies, rotation sensors should reach approximately the same signal-to-noise ratio as classically used seismometers that measure translational ground motion.

5.2. Physical Origin of the Information Gain
Probabilistic inversion does not directly provide a physical explanation for an observed information gain. It seems plausible, however, that the horizontal rotation components make a significant contribution. Horizontal ground rotations carry information on the vertical displacement gradient, thereby providing information that cannot be obtained from conventional 3-C recordings on the Earth's surface. It follows that a potentially positive information gain from the incorporation of rotational ground motions may be even more significant for events that fracture as well in the vertical direction (dip slip), thereby producing larger horizontal rotation.

5.3. Implications for Earthquake Physics and Ground Motion Predictions
In our analysis the incorporation of rotational ground motions is most beneficial for the resolution of rupture velocity and rise time, i.e., those parameters that are nonlinearly related to ground motion [*Archuleta*, 1984]. Accurate knowledge of both rupture velocity and rise time is critical for the inference of rheological fault properties and rupture dynamics [e.g., *Tinti et al.*, 2009].
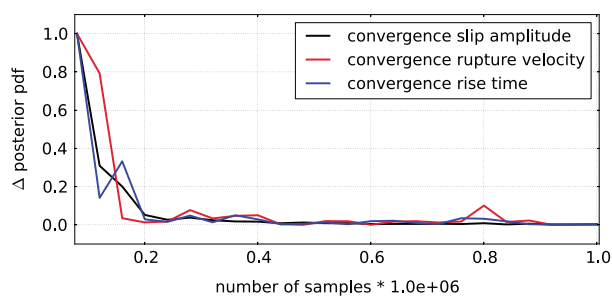
Figure 10. Convergence of the Metropolis-Hastings sampling algorithm. The change of the marginal *posterior pdf*s for slip amplitude (black line), the rupture velocity (red line), and the rise time (blue line) are plotted as a function of accumulated samples.

Rupture velocity controls the directivity effect which increases ground motions normal to the fault [e.g., *Somerville et al.*, 1997]. Furthermore, far-field displacement depends on the moment time derivative, meaning that ground motions depend strongly on the rise time. In this context, the incorporation of rotational ground motions has the potential to improve estimates of parameters that are critical for earthquake-induced ground motion. Nevertheless, further investigations must evaluate the performance of rotational ground motions also in more complex rupture scenarios. The study by *Razafindrakoto and Mai* [2014], for example, suggests to test more sophisticated source time functions as a next step.

5.4. Probabilistic Source Inversion

Probabilistic inversion bring numerous advantages that are critical for our study, including the absence of linearization and regularization, the nearly exhaustive exploration of the model space, and the possibility to obtain comprehensive information on uncertainties and trade-offs. Critical aspects of probabilistic inversion are the choice of a prior and the convergence of the sampling algorithm.

The incorporation of prior knowledge is a controversially debated component of Bayesian inversion [e.g., *Efron*, 2013]. It must, most importantly, be acknowledged that any inference is relative to the prior, and this prior must be taken into account when interpreting the results. In our case it is reasonable to model the available prior knowledge in terms of a flat *prior pdf* that reflects a low level of knowledge. The impact of this choice is, however, small because we are primarily interested in the comparison of the information gain of various scenarios with identical priors.

To assess the convergence of the Metropolis-Hastings algorithm, we monitor the change of the marginal *posterior pdf*s as a function of the total number of samples. This is displayed in Figure 10 for scenario II (section 4.2). After approximately 250,000 samples, i.e., 25% of the total 1 million samples, the observed changes in the *posterior pdf*s are practically negligible. This indicates that the sampling process indeed converges to the *posterior pdf*. In scenario I, we observed a comparable convergence behavior. Furthermore, we note that various independently repeated runs resembled the *posterior pdf*s presented in both scenarios. Thus, we can assume that our results are not affected by the starting model of the sampling process.

6. Conclusions

Based on a series of Bayesian finite source inversions, we assess the potential of rotational ground motion recordings to reduce nonuniqueness in kinematic source parameters. Our results suggest that the incorporation of rotational ground motion recordings can significantly reduce nonuniqueness in finite source inversions when measurement uncertainties are approximately similar to or below the uncertainties of translational velocity recordings. This requirement should be met by currently developed rotation sensors in order to be useful in finite source studies. Rupture velocity and rise time have the highest potential to benefit from rotation data. The trade-offs between both parameters can be strongly reduced, and the information gain significantly increased. It follows that rotation data can improve secondary inferences that depend on rupture velocity and rise time, such as radiation directivity and frictional properties of the fault. The reduced nonuniqueness most likely results from the horizontal rotation components that carry information on the vertical displacement velocity gradient that cannot be derived from translation recordings at the surface.

Appendix A: One-Dimensional Earth Model

For the computation of the seismic wavefield for the moment tensor point sources, we use the 1-D Earth model from *Semmane et al.* [2005] (Table A1):

Table A1. Description of the Layered Earth Model
Used for the Wavefield Computations

Depth (km)	V_p (km/s)	V_s (km/s)	ρ (kg/m^3)
0	5.50	3.179	2600
2	6.05	3.497	2700
16	6.60	3.815	2800
38	8.03	4.624	3100

Appendix B: Source Function

In this study the source function is constructed as an ordinary ramp function. In the time domain and as a function of the rise time R the ramp function is expressed as

$$\tilde{S}(R, t) = \begin{cases} 0, & t < 0 \\ t/R, & 0 \leq t \leq R \\ 1, & t > R. \end{cases}$$

The representation in the frequency domain can then be computed as

$$S(R, \omega) = \mathcal{F}[\frac{d}{dt}\tilde{S}](\omega)\frac{1}{i\omega} = \frac{1}{w^2 R}[\exp(-i\omega R) - 1]$$

where $\mathcal{F}$ denotes the Fourier transform of $\frac{d}{dt}\tilde{S}$.

Appendix C: Plausible Model Solutions for Scenario II From Section 4.2

Highlighting some characteristic features of probabilistic inversion, this appendix aims to evaluate the ensemble of models accepted during the inversion process of scenario II from section 4.2.
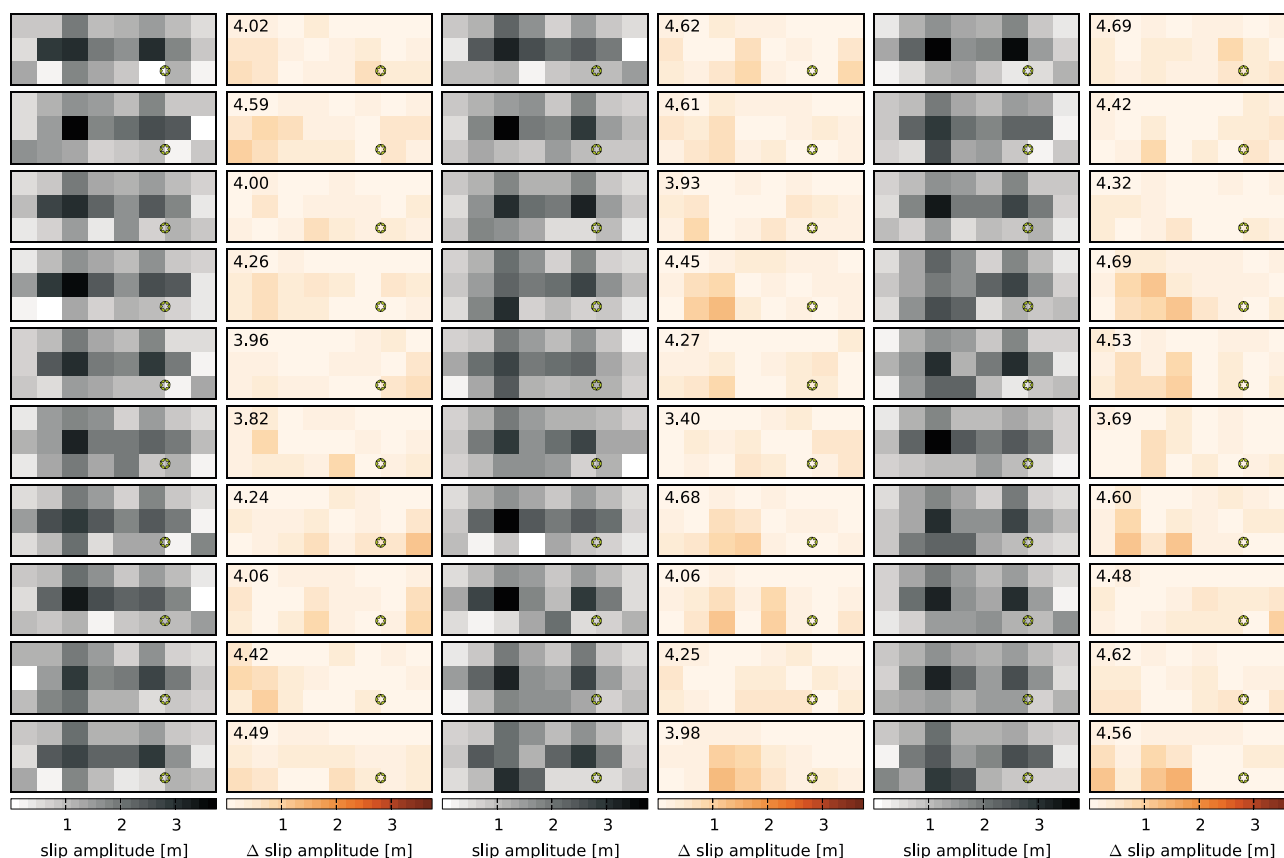

Figure C1. (first, third, and fifth columns) Thirty slip amplitude models randomly picked from the 10,000 best data fitting models in the sampled ensemble. (second, fourth, and sixth columns) The quantified corresponding discrepancies between the slip amplitudes of each subfault compared to the target model. The numbers indicate the L_2 misfit between the individual models and the target model depending on slip amplitudes, rupture velocity, and rise time.
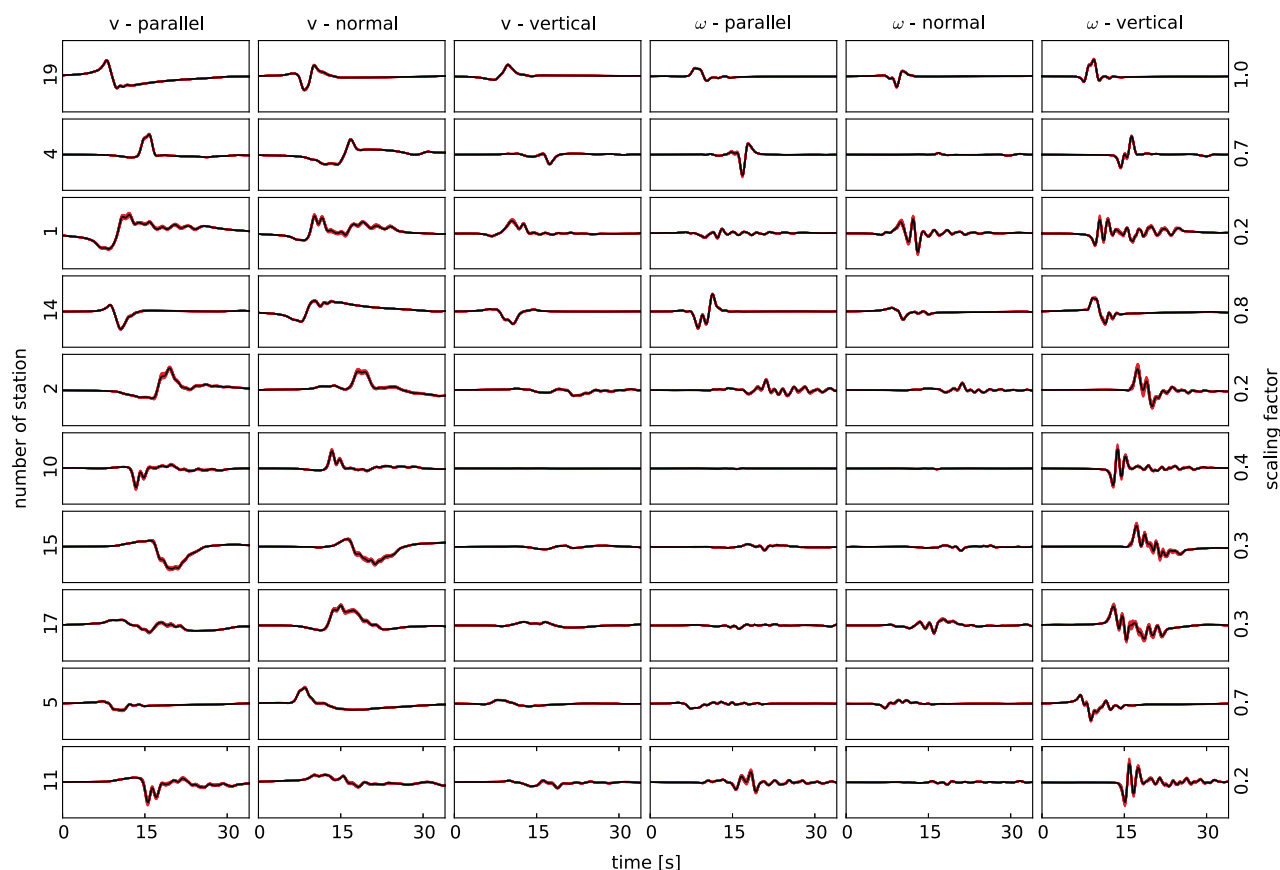
Figure C2. (left to right) Fault parallel, fault normal, and vertical velocity followed by rotation rate seismograms in the same order. In each panel black lines represent observations, while red lines correspond to the simulated seismograms of all 30 models from Figure C1. Each row corresponds to one of the 10 stations selected in scenario II. The normalized scaling factor to the right encodes the strength of the signal at each station. Note that a decreasing scaling factor corresponds to smaller amplitudes. According to that, the highest amplitudes are observed at station 19.

To acquire intuition for the variability of plausible models, 30 of the 10,000 best data fitting models were randomly selected. These are displayed in Figure C1 together with their respective deviations from the target model. While the data misfits of most models fall within the narrow range of 4.2 ± 0.2, significant variability exists for those subfaults where the information gain is comparatively low, i.e., at greater depth and near the northwestern tip of the fault plane.

In Figure C2 each column corresponds to one component of the 6-C observations and each row represents one of the 10 stations randomly selected in scenario II. The normalized scaling factor encodes the strength of the signal at each station. While decreasing scaling factors correspond to smaller amplitudes, the highest amplitudes are observed in station 19. Figure C2 indicates, as expected, that seismograms with high energy at stations close to the fault, e.g., stations 4, 5, 14, and 19 (see Figure 3) are fitted best while slightly larger variations are observed for stations recording lower amplitudes (e.g., stations 1, 2, and 11). The fact that different models produce similar seismograms despite considerable variations concerning individual parameters expresses the nonuniqueness of the inverse problem and reflects the trade-offs between the model parameters and the observations. For example, the slip amplitudes of the first model plotted in Figure C1 (fifth column) resemble the target model, while, despite of a smaller L_2 misfit value, the slip amplitudes of the last model in the third column miss the target model concerning the slip amplitudes of several subfaults. This is possible because the misfit depends also on the values for the rupture velocity and the rise time, and it demonstrates the problem of providing a single model as the solution of probabilistic inverse scenarios.

References

Aki, K., and P. Richards (2002), *Quantitative Seismology*, University Science Books, Sausalito, Calif.

Archuleta, R. J. (1984), A faulting model for the 1979 Imperial Valley earthquake, *J. Geophys. Res.*, *89*, 4559–4585.

Beresnev, I. A. (2003), Uncertainties in finite-fault slip inversions: To what extent to believe? (A critical review), *Bull. Seismol. Soc. Am.*, *93*, 2445–2458.

Bernauer, F., J. Wassermann, and H. Igel (2012a), Rotational sensors—A comparison of different sensor types, *J. Seismol.*, *16*, 595–602, doi:10.1007/s10950-012-9286-7.

Bernauer, M., A. Fichtner, and H. Igel (2009), Inferring earth structure from combined measurements of rotational and translational ground motions, *Geophysics*, *74*, WCD41–WCD47.

Bernauer, M., A. Fichtner, and H. Igel (2012b), Measurements of translation, rotation and strain: New approaches to seismic processing and inversion, *J. Seismol.*, *16*, 669–681.

Bodin, P., J. Gomberg, S. K. Singh, and M. Santoyo (1997), Dynamic deformations of shallow sediments in the Valley of Mexico. Part I: Three-dimensional strains and rotations recorded on a seismic array, *Bull. Seismol. Soc. Am.*, *87*, 528–539.

Brokešová, J., and J. Málek (2010), New portable sensor system for rotational seismic motion measurements, *Rev. Sci. Instrum.*, *81*(8), 084,501, doi:10.1063/1.3463271.

Brokešová, J., J. Málek, and P. Kolínský (2012), Rotaphone, a mechanical seismic sensor system for field rotation rate measurements and its in situ calibration, *J. Seismol.*, *16*, 603–621.

Cochard, A., H. Igel, B. Schuberth, W. Suryanto, A. Velikoseltsev, U. Schreiber, J. Wassermann, F. Scherbaum, and D. Vollmer (2006), Rotational motions in seismology: Theory, observation, simulation, in *Earthquake Source Asymmetry, Structural Media and Rotation Effects*, edited by R. Teisseyre, M. Takeo, and E. Majewski, Springer, Heidelberg, Germany.

Cotton, F., and M. Campillo (1994), Application of seismogram synthesis to the study of earthquake source from strong motion records, *Ann. Geofis.*, *37*(6), 1539–1564.

Cotton, F., and M. Campillo (1995), Frequency domain inversion of strong motions: Application to the 1992 Landers earthquake, *J. Geophys. Res.*, *100*, 3961–3975, doi:10.1029/94JB02121.

Custodio, S., P. Liu, and R. J. Archuleta (2005), The 2004 M_w6.0 Parkfield, California, earthquake: Inversion of near-source ground motion using multiple data sets, *Geophys. Res. Let.*, *32*, L23312, doi:10.1029/2005GL024417.

Efron, B. (2013), Bayes' theorem in the 21st century, *Science*, *340*, 1177–1178, doi:10.1126/science.1236536.

Fichtner, A., and H. Igel (2009), Sensitivity densities for rotational ground motion measurements, *Bull. Seismol. Soc. Am.*, *99*, 1302–1314.

Fichtner, A., and H. Tkalcic (2010), Insights into the kinematics of a volcanic caldera drop: Probabilistic finite-source inversion of the 1996 Bardarbunga, Iceland, earthquake, *Earth Planet. Sci. Lett.*, *297*, 607–615.

Fichtner, A., B. L. N. Kennett, H. Igel, and H.-P. Bunge (2009), Spectral-element simulation and inversion of seismic waves in a spherical section of the Earth, *J. Numer. Anal. Ind. Appl. Math.*, *4*, 11–22.

Fukuyama, E., W. L. Ellsworth, F. Waldhauser, and A. Kubo (2003), Detailed fault structure of the 2000 western Tottori, Japan, earthquake sequence, *Bull. Seismol. Soc. Am.*, *93*, 1468–1478.

Hartzell, H. S., and T. H. Heaton (1983), Inversion of strong ground motion and teleseismic waveform data for the fault rupture history of the 1979 Imperial Valley, California, earthquake, *Bull. Seismol. Soc. Am.*, *73*, 1553–1583.

Hartzell, S., P. Liu, C. Mendoza, C. Ji, and K. M. Larson (2007), Stability and uncertainty of finite-fault slip inversions: Application to the 2004 Parkfield, California, earthquake, *Bull. Seismol. Soc. Am.*, *97*, 1911–1934, doi:10.1785/0120070080.

Hastings, W. K. (1970), Monte Carlo sampling methods using Markov chains and their applications, *Biometrika*, *57*, 97–109.

Hernandez, B., F. Cotton, and M. Campillo (1999), Contribution of radar interferometry to a two-step inversion of the kinematic process of the 1992 Landers earthquake, *J. Geophys. Res.*, *104*, 13,083–13,099, doi:10.1029/1999JB900078.

Ide, S., G. C. Beroza, and J. J. McGuire (2005), Imaging earthquake source complexity, in *Seismic Earth: Array Analysis of Broadband Seismograms*, vol. 157, edited by A. Levander and G. Nolet, pp. 117–135, AGU, Washington, D. C.

Igel, H., U. Schreiber, A. Flaws, B. Schuberth, A. Velikoseltsev, and A. Cochard (2005), Rotational motions induced by the M 8.1 Tokachi-Oki earthquake, September 25, 2003, *Geophys. Res. Lett.*, *32*, L08309, doi:10.1029/2004GL022336.

Igel, H., A. Cochard, J. Wassermann, A. Flaws, U. Schreiber, A. Velikoseltsev, and N. P. Dinh (2007), Broad-band observations of earthquake-induced rotational ground motions, *Geophys. J. Int.*, *168*, 182–196, doi:10.1111/j.1365-246X.2006.03146.x.

Iwata, T., and H. Sekiguchi (2002), Source processes and near-source ground motion during the 2000 Tottori-ken Seibu earthquake, *paper presented at 11th Japan Earthquake Engineering Symposium, Earthquake Eng. Res. Liaison Comm., Sci. Counc. of Jpn.*, Tokyo, Japan.

Kendall, L. M., C. A. Langston, W. H. K. Lee, C.-J. Lin, and C.-C. Liu (2012), Comparison of point and array-computed rotations for the TAIGER explosions of 4 March 2008, *J. Seismol.*, *16*, 733–743, doi:10.1007/s10950-012-9297-4.

Mai, M., J. Burjanek, B. Delouis, G. Festa, C. Francois-Holden, D. Monelli, T. Uchide, and J. Zahradnik (2007), Earthquake source inversion blindtest: Initial results and further developments, *Eos Trans. AGU*, *88*(52), Fall Meet. Suppl., Abstract S53C-08.

Mendoza, C., and S. H. Hartzell (1989), Slip distribution of the 19 September 1985 Michoacan, Mexico, earthquake: Near-source and teleseismic constraints, *Bull. Seismol. Soc. Am.*, *79*, 655–669.

Metropolis, N., and S. Ulam (1949), The Monte Carlo method, *J. Am. Stat. Assoc.*, *44*, 335–341.

Metropolis, N., M. N. Rosenbluth, A. W. Rosenbluth, A. H. Teller, and E. Teller (1953), Equation of state calculations by fast computing machines, *J. Chem. Phys.*, *21*, 1087–1092.

Monelli, D., and P. M. Mai (2008), Bayesian inference of kinematic earthquake rupture parameters through fitting of strong motion data, *Geophys. J. Int.*, *173*, 220–232, doi:10.1111/j.1365-246X.2008.03733.x.

Monelli, D., P. M. Mai, S. Jónsson, and D. Giardini (2009), Bayesian imaging of the 2000 western Tottori (Japan) earthquake through fitting of strong motion and GPS data, *Geophys. J. Int.*, *176*, 135–150, doi:10.1111/j.1365-246X.2008.03943.x.

Mosegaard, K., and A. Tarantola (1995), Monte Carlo sampling of solutions to inverse problems, *J. Geophys. Res.*, *100*, 12,431–12,447, doi:10.1029/94JB03097.

Olson, A. H., and J. Anderson (1988), Implications of frequency-domain inversion of earthquake ground motions for resolving the space-time dependence of slip on an extended fault, *Geophys. J. Int.*, *94*, 443–455.

Olson, A. H., and R. J. Apsel (1982), Finite faults and inverse theory with applications to the 1979 Imperial Valley earthquake, *Bull. Seismol. Soc. Am.*, *72*, 1969–2001.

Peyrat, S., and K. B. Olsen (2004), Nonlinear dynamic rupture inversion of the 2000 western Tottori, Japan, earthquake, *Geophys. Res. Let.*, *31*, L05604, doi:10.1029/2003GL019058.

Pham, D. N., B.-S. Huang, C.-J. Lin, T.-M. Vu, and N.-A. Tran (2012), Investigation of ground rotational motions caused by direct and scattered P-waves from the 4 March 2008 TAIGER explosion experiment, *J. Seismol.*, *16*, 709–720, doi:10.1007/s10950-012-9300-0.

Piatanesi, A., A. Cirella, P. Spudich, and M. Cocco (2007), A global search inversion for earthquake kinematic rupture history: Application to the 2000 western Tottori, Japan earthquake, *J. Geophys. Res.*, *112*, B07314, doi:10.1029/2006JB004821.

Razafindrakoto, H. N. T., and P. M. Mai (2014), Uncertainty in earthquake source imaging due to variations in source time function and earth structure, *Bull. Seismol. Soc. Am.*, *104*, 855–874, doi:10.1785/0120130195.

Sambridge, M. S., and K. Mosegaard (2002), Monte Carlo methods in geophysical inverse problems, *Rev. Geophys.*, *40*, 1009, doi:10.1029/2000RG000089.

Schreiber, K. U., A. Velikoseltsev, A. J. Carr, and R. Franco-Anaya (2009a), The application of fiber optic gyroscopes for the measurement of rotations in structural engineering, *Bull. Seismol. Soc. Am.*, *99*, 1207–1214, doi:10.1785/0120080086.

Schreiber, U., J. N. Hautmann, A. Velikoseltsev, J. Wassermann, H. Igel, J. Otero, F. Vernon, and J.-P. R. Wells (2009b), Ring laser measurements of ground rotations for seismology, *Bull. Seismol. Soc. Am.*, *99*, 1190–1198, doi:10.1785/0120080171.

Semmane, F., F. Cotton, and M. Campillo (2005), The 2000 Tottori earthquake: A shallow earthquake with no surface rupture and slip properties controlled by depth, *J. Geophys. Res.*, *110*, B03306, doi:10.1029/2004JB003194.

Somerville, P. G., N. F. Smith, R. W. Graves, and N. A. Abrahamson (1997), Modification of empirical strong ground motion attenuation relations to include the amplitude and duration effects of rupture directivity, *Seismol. Res. Lett.*, *68*, 199–222.

Spudich, P., and J. B. Fletcher (2008), Observation and prediction of dynamic ground strains, tilts, and torsions caused by the Mw 6.0 2004 Parkfield, California, earthquake and aftershocks, derived from UPSAR array observations, *Bull. Seismol. Soc. Am.*, *98*, 1898–1914, doi:10.1785/0120070157.

Spudich, P., L. K. Steck, M. Hellweg, J. B. Fletcher, and L. M. Baker (1995), Transient stresses at Parkfield, California, produced by the M 7.4 Landers earthquake of June 28, 1992: Observations from the UPSAR dense seismograph array, *J. Geophys. Res.*, *100*(B1), 675–690, doi:10.1029/94JB02477.

Stupazzini, M., J. de la Puente, C. Smerzini, M. Käser, H. Igel, and A. Castellani (2009), Study of rotational ground motion in the near-field region, *Bull. Seismol. Soc. Am.*, *99*, 1271–1286, doi:10.1785/0120080153.

Suryanto, W., H. Igel, J. Wassermann, A. Cochard, B. Schuberth, D. Vollmer, F. Scherbaum, U. Schreiber, and A. Velikoseltsev (2006), First comparison of array-derived rotational ground motions with direct ring laser measurements, *Bull. Seismol. Soc. Am.*, *99*, 2059–2071, doi:10.1785/0120060004.

Takeo, M., and H. M. Ito (1997), What can be learned from rotational motions excited by earthquakes?, *Geophys. J. Int.*, *129*, 319–329.

Takeo, M. (1998), Ground rotational motions recorded in near-source region of earthquakes, *Geophys. Res. Let.*, *25*, 789–792, doi:10.1029/98GL00511.

Tarantola, A. (2005), *Inverse Problem Theory and Methods for Model Parameter Estimation,* 2nd ed., Society for Industrial and Applied Mathematics, Philadephia, Penn.

Tinti, E., M. Cocco, E. Fukuyama, and A. Piatanesi (2009), Dependence of slip weakening distance (D_c) on final slip during dynamic rupture of earthquakes, *Geophys. J. Int.*, *177*, 1205–1220.

Trampert, J., and A. Fichtner (2013), Global imaging of the Earth's deep interior: Seismic constraints on (an)isotropy, density and attenuation, in *Physics and Chemistry of the Deep Earth*, edited by S. Karato, Wiley, Hoboken, N. J.

Velikoseltsev, A., K. U. Schreiber, A. Yankovsky, J.-P. R. Wells, A. Boronachin, and A. Tkachenko (2012), On the application of fiber optic gyroscopes for detection of seismic rotations, *J. Seismol.*, *16*, 623–637, doi:10.1007/s10950-012-9282-y.

Wald, D. J., and T. H. Heaton (1994), Spatial and temporal distribution of slip for the 1994 Landers, California earthquake, *Bull. Seismol. Soc. Am.*, *84*, 668–691.

Wang, H., H. Igel, F. Gallovic, and A. Cochard (2009), Source and basin effects on rotational ground motions: Comparison with translations, *Bull. Seismol. Soc. Am.*, *99*, 1162–1173, doi:10.1785/0120080115.

Zembaty, Z. (2009), Rotational seismic load definition in eurocode 8, part 6 for slender tower-shaped structures, *Bull. Seismol. Soc. Am.*, *99*, 1483–1485, doi:10.1785/0120080252.